ADVANCED MATERIALS
www.advmat.de

Manipulating Color Emission in 2D Hybrid Perovskites by Fine Tuning Halide Segregation: A Transparent Green Emitter

*Andrea Zanetta, Zahra Andaji-Garmaroudi, Valentina Pirota, Giovanni Pica, Felix Utama Kosasih, Laxman Gouda, Kyle Frohna, Caterina Ducati, Filippo Doria, Samuel D. Stranks, and Giulia Grancini**

Halide perovskite materials offer an ideal playground for easily tuning their color and, accordingly, the spectral range of their emitted light. In contrast to common procedures, this work demonstrates that halide substitution in Ruddlesden–Popper perovskites not only progressively modulates the bandgap, but it can also be a powerful tool to control the nanoscale phase segregation—by adjusting the halide ratio and therefore the spatial distribution of recombination centers. As a result, thin films of chloride-rich perovskite are engineered—which appear transparent to the human eye—with controlled tunable emission in the green. This is due to a rational halide substitution with iodide or bromide leading to a spatial distribution of phases where the minor component is responsible for the tunable emission, as identified by combined hyperspectral photoluminescence imaging and elemental mapping. This work paves the way for the next generation of highly tunable transparent emissive materials, which can be used as light-emitting pixels in advanced and low-cost optoelectronics.

1. Introduction

In the last decade hybrid perovskites have been widely explored as promising active material for high performance solar cells and light-emitting devices (LEDs), nowadays reaching efficiency values approaching those of state-of-the-art technologies based on traditional semiconductors.[1–4] The facile tunability of their electronic and structural properties upon chemical manipulation is certainly one of the key characteristics that makes this material family a versatile object for many different applications. In particular, tuning the material bandgap by halide substitution has been from the very beginning a powerful strategy to obtain hybrid perovskites with different colors and tunable emission.[5] This stems true for the ubiquitous ABX_3 perovskite (or 3D in the following), but it also extends to lower-dimensional systems.[5,6] For instance, by incorporating large cations in the A site, layered 2D perovskites (2DPs) can be formed, an interesting playground class of materials with superior stability with respect to more widely used 3D hybrid perovskites.[7] In addition, their unique optical properties, including quantum and dielectric confinement, Rashba splitting, and large exciton binding energy, make them attractive for different fields beyond light-emitting applications, such as spintronics, imaging, and scintillators.[8–13]

The general formula of Ruddlesden–Popper perovskites is $R_2A_{n-1}B_n X_{3n+1}$ in which A is typically an organic cation (methylammonium, MA^+), B a divalent metal species such as Pb^{2+}, X a halogen monovalent anion (I^-, Br^-, Cl^-), and R a large organic spacer cation. The R cation usually contains an alkyl chain capable to isolate the inorganic octahedra of the perovskite in *n*-dimensional sheets; the framework of these 2DP can be described as a quantum well system in which the organic cations is able to space the semiconductive sheets in a confined dimension (see cartoon of **Figure 1**a).[7] For these materials, the optical properties and their excitonic nature are influenced by the confined nature of the inorganic sheets that compose their layered structure.[7,9]

Similar to the 3D case, changing the halide from I^- to Br^- and Cl^-, the optical bandgap increases and the optical properties

A. Zanetta, Z. Andaji-Garmaroudi, V. Pirota, G. Pica, L. Gouda, F. Doria, G. Grancini
Department of Chemistry & INSTM
Università di Pavia
Via T. Taramelli 14, Pavia 27100, Italy
E-mail: giulia.grancini@unipv.it
Z. Andaji-Garmaroudi, K. Frohna, S. D. Stranks
Cavendish Laboratory
University of Cambridge
JJ Thomson Avenue, Cambridge CB3 0HE, UK
F. U. Kosasih, C. Ducati
Department of Materials Science and Metallurgy
University of Cambridge
27 Charles Babbage Road, Cambridge CB3 0FS, UK
S. D. Stranks
Department of Chemical Engineering and Biotechnology
University of Cambridge
Cambridge CB3 0AS, UK
The ORCID identification number(s) for the author(s) of this article can be found under https://doi.org/10.1002/adma.202105942.

DOI: 10.1002/adma.202105942

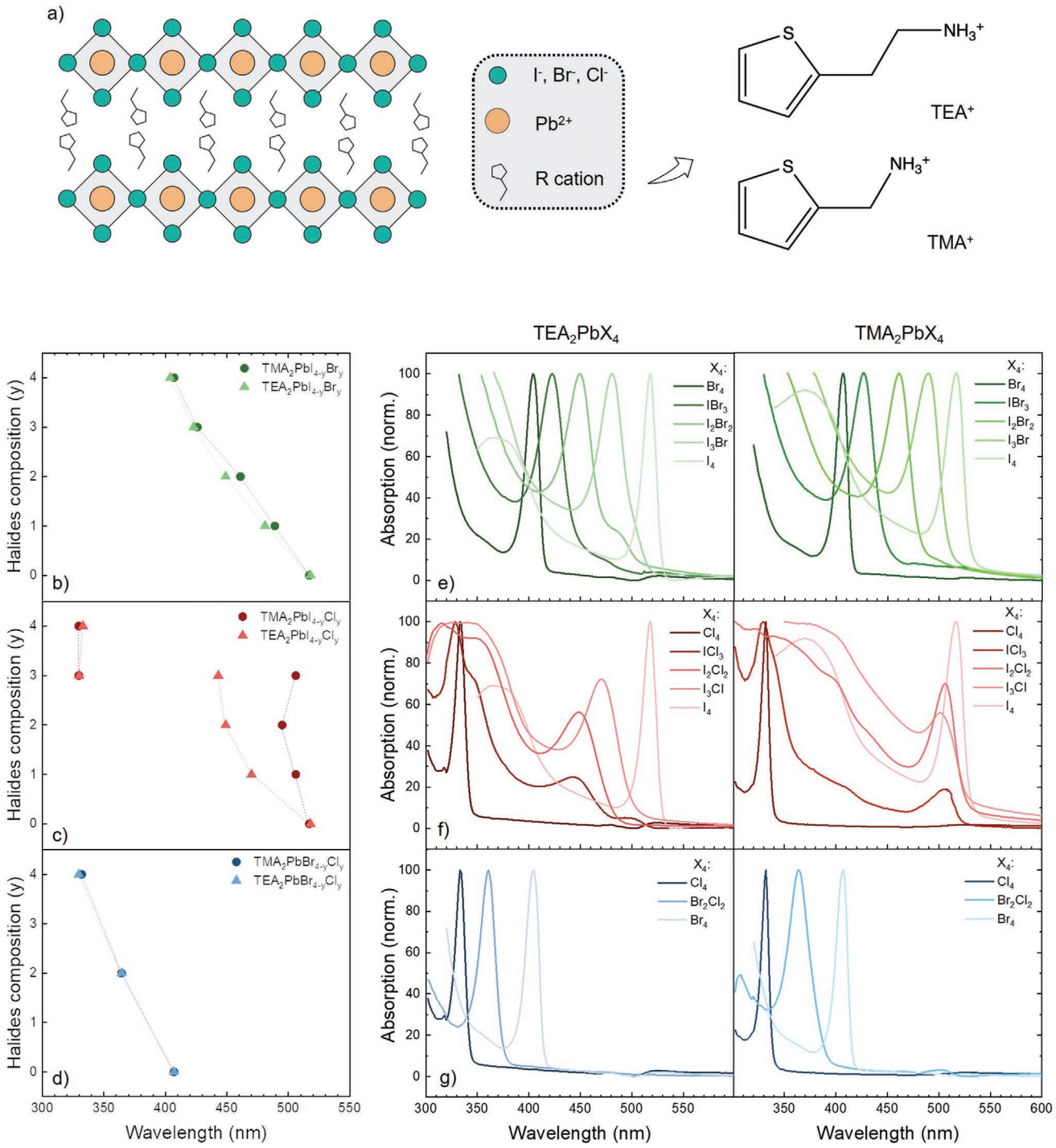

Figure 1. a) Cartoon representing the 2DP framework in which the inorganic perovskite octahedra layers are separated by the presence of the long-chain organic cations (R). The structures of the two different R spacer cations investigated in this work are also shown: TEA^+ and TMA^+. b–d) The three vertically stacked panels show the position of the absorption peaks of the different materials prepared as a function of the halide composition; (a) refers to the I–Br mixture for both TMA and TEA, (b) to I–Cl mixtures, and (c) to Br–Cl mixtures. The dotted lines represent connecting guides to the eye. e–g) UV–vis absorption spectra of all the materials analyzed. TEA- and TMA-based materials are represented in the left and right of the panels, respectively. e) The I–Br mixtures, f) the I–Cl mixtures, and g) the Br–Cl mixtures. From the analysis of these data the panels in (b)–(d) have been constructed.

such as absorption and photoluminescence undergo a corresponding blueshift.[14] Although this approach has already been widely exploited for tuning the bandgap and stabilizing 3D hybrid perovskites materials, little has been done for the case of low-dimensional perovskites.[15–18] In the case of 2DPs, the mixed halide compositions have been only explored by

mixing iodide–bromide and bromide–chloride species.[16,18–22] Br–Cl mixtures of 2DP materials have been recently studied in order to develop white-light LEDs by exploiting the light emission from self-trapped excitons formed in the distorted Br–Cl low-dimensional phase:[20,21,23] in fact, due to the layered structure of these materials, the distortions induced by the different halide substitution are enhanced leading to the formation of broad light emission, as in the case of Br–Cl mixtures, or even phase separation.[20,21,24,25] For 2DPs comprised of I–Br halides mixture, working LEDs have been recently studied:[19,26] the high voltage necessary for their functioning favors halides migration, and subsequent formation of zones in which halides are inevitably segregated. Hence, in most cases, uncontrolled halide migration and separation in different phases are observed, which makes their manipulation and their direct implementation into working devices highly challenging.

In this work, we explored a series of 2DPs by halide substitution in combination with the use of two different R long-chain organic cations, resulting in the formation of $R_2PbI_{4-\gamma}Br_\gamma$, $R_2PbI_{4-\gamma}Cl_\gamma$, and $R_2PbBr_{4-\gamma}Cl_\gamma$ materials. We demonstrated that halide substitution does not only progressively impact the bandgap modulation, but it is also a powerful tool to manipulate the nanoscale halide phase segregation and, concomitantly, the formation of multiple subphases. The choice of the organic cation plays a key role in controlling the dimension of the microdomains and therefore of the spatial distribution of the recombination on these small length scales. Specifically, the microscale distribution results from the segregation of phases with different iodide and chloride content: the different ionic radius limits the miscibility of these halides, inducing microaggregates with different compositions. For I–Cl mixtures with Cl contents higher than 50%, a predominant chloride-rich phase determines the main optical absorption of the material in the UV, leading to the formation of a quasi-transparent film. Upon excitation, energy funnels into the minority iodide-rich domains on which intense green emission occurs. Our approach creates a material transparent to the visible eye, but able to emit in the green, opening the path for the development of new generation of light-emitting devices based on multiphases transparent perovskites materials.

2. Experimental Results

2.1. Optical Absorption Properties

Halide substitution is a powerful method for the modulation of the optical properties of 2D perovskites.[14,18] In this work, both pure and mixed halide compositions are studied: the composition of the materials is expressed by the formula $R_2PbX_{4-\gamma}X'_\gamma$. R is a long-chain cation based on thiophene moieties (2-thiophene ethyl ammonium$^+$ and 2-thiopene methyl ammonium$^+$- TEA and TMA, respectively) whose structural formula is reported in Figure 1a, which we synthesized following a previously reported method.[27] This results in the development of two families of 2DPs: TMA- and TEA-based, respectively. For each class, X and X′, different halides species (I^-, Br^-, and Cl^- and mixtures thereof) have been used. By changing the stoichiometry of the precursors, it is possible to obtain either materials with pure halide (γ = 0, 4) or mixed compositions (γ = 1, 2, 3). The resulting mutual interaction and self-organization of the halides leads to tunable optical, structural, and morphological properties.

Figure 1b–g shows the optical properties of TMA- and TEA-based 2DPs with all the different halides compositions analyzed. The data in Figure 1b–d represent the position of the excitonic absorption peak, extracted from UV–vis absorption spectra (reported in Figure 1e–g) as a function of halide mixture. By looking at the absorption peak positions, two different trends are clearly distinguishable: i) for $R_2PbI_{4-\gamma}Br_\gamma$ and $R_2PbBr_{4-\gamma}Cl_\gamma$ (Figure 1b,d), a gradual shift of the main absorption peak position is observed by increasing the content of the γ-host halide. This blueshift follows a linear variation indicating a fine control of the bandgap tunability by engineering the halide composition. A similar blueshift trend is also visible in the photoluminescence spectra (Figure S1, Supporting Information), indicating the possibility to control the light emission properties of these mixed halides materials in the 400–550 nm region of the visible spectra. ii) for $R_2PbI_{4-\gamma}Cl_\gamma$ (Figure 1c) the scenario is completely different. By increasing the content of Cl^- the absorption peak does not undergo a linear blueshift as in the previous case, but the absorption persists in the 490–520 nm region. Surprisingly, at a threshold chlorine concentration higher than 50% (γ > 2) multiple distinct absorption peaks appear, for both the TEA- and TMA-based materials. This result suggests the formation of different phases related to nonuniform halide distributions inside the $R_2PbI_{4-\gamma}Cl_\gamma$ material. We propose there is formation of an iodide–chloride mixed phase, with a high content of I^-, that absorbs ≈500 nm and a chlorine rich-region absorbing in the UV spectral region. Interestingly, the different organic cation also plays a role: looking at the absorption spectra, TEA-based materials show a slight blueshift in the main absorption peak position passing from γ = 0 to γ = 2, with respect to the case of TMA analogues. This suggests that the TEA can accommodate a larger incorporation of the Cl^- atom inside the iodide–chloride mixed phase before undergoing segregation.

2.2. Structural X-ray Diffraction Analysis

To corroborate our findings, we measured the X-ray diffraction (XRD) patterns of the films. **Figure 2** shows XRD patterns for the different materials; complete patterns are shown in Figure S2 of the Supporting Information. Notably, the patterns consist of a main peak at low diffraction angle, the fingerprint of the 2D perovskite phase.[27] Also in this case, different trends are clearly distinguishable: i) for $R_2PbI_{4-\gamma}Br_\gamma$ the XRD peak undergoes a gradual shift for higher Br content to lower (higher) angles for TMA- (TEA-) based system, respectively. The different trend of peak shift is possibly due to the different distortion upon halide mixing induced by the different character—in term of rigidity—of the framework; ii) for $R_2PbI_{4-\gamma}Cl_\gamma$ TEA- and TMA-based materials again behave differently. For the TEA-based cation a gradual shift is observed. However, at closer inspection, we observe a broadening of the main peak. For the TMA-based system the mixture of I–Cl results in the formation of two distinct peaks corresponding to the ones of the pure

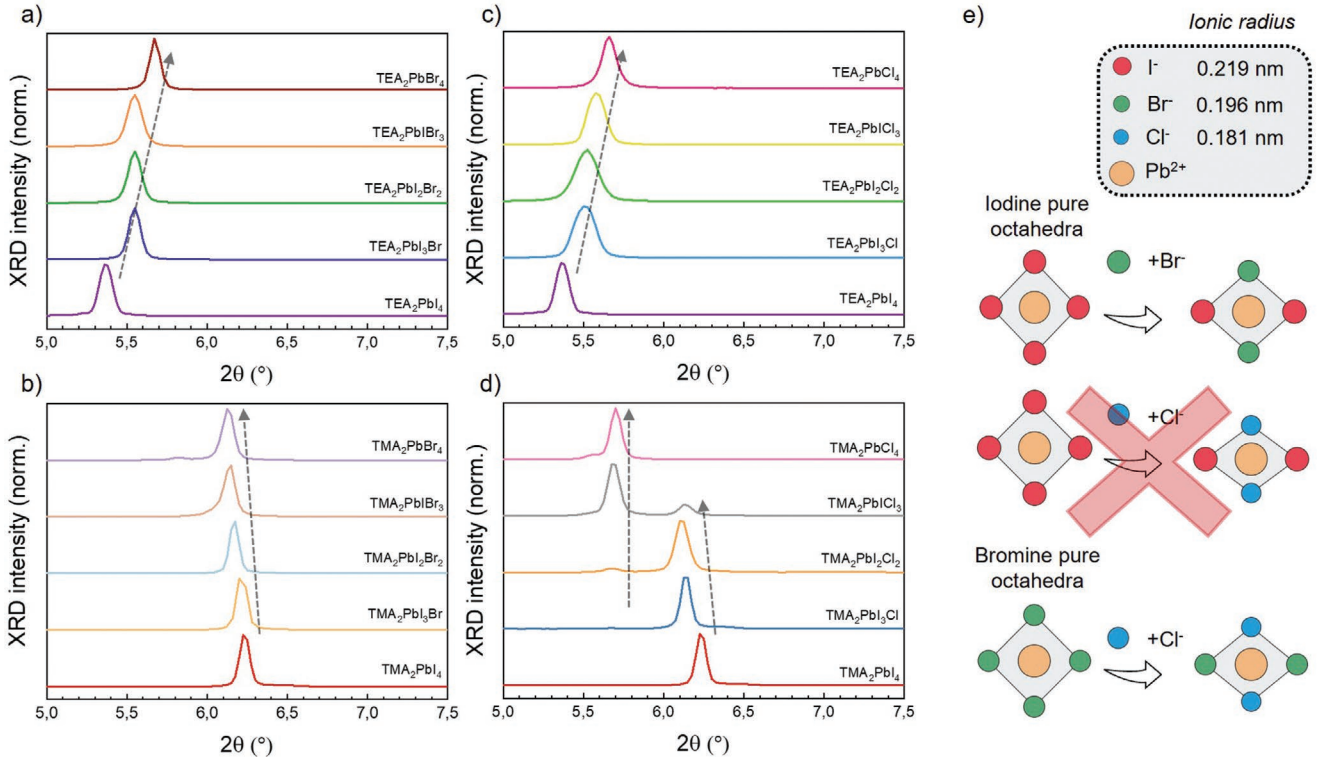

Figure 2. a–d) X-ray diffraction patterns for the $R_2PbI_{4-y}Br_y$ (a,b) and $R_2PbI_{4-y}Cl_y$ (c,d) materials in the 5°–7.5° 2θ range (patterns in the wider 3°–35° range are depicted in Figure S3, Supporting Information). The dotted eye-guide lines in the graphs highlight the path followed by the diffraction peak by increasing the amount of the host halide inside the material. In (a–c), a linear trend in the shift of the peak with the change of the materials' stoichiometry (a visible broadening of the peak in (c)) is visible for intermediate compositions), while in (d) the growth of different peaks related to different segregated phase is addressed, as indicated by the two dotted arrows. e) The cartoon represents the mechanism that governs the phase segregation due to mixed halides composition. As drawn, Br (Cl) can be hosted inside the I (Br) perovskite inorganic octahedra without exceeding distortions in the lattice. On the contrary, in case of I–Cl mixture, due to the huge difference in ionic radius between the two species, the iodine octahedra cannot accommodate Cl atoms without massive distortion; hence, the material prefers to segregate in two distinct phases.

halide phases (I pure, Cl pure). We can rationalize our results as follows: depending on the halide and on the organic cation used, the 2D framework experiences a shrinkage or enlargement of the unit cell, leading to a shift in the 2θ position of the XRD peaks. This happens in all cases, except for the TMA-based I–Cl mixture, where the distinct peaks are related to the concomitant presence of two different phases related to pure TMA_2PbCl_4 and a mixed iodide–chloride phase, made up predominantly of the iodide species. By continuously increasing the chlorine content in the material the relative intensity of the two peaks changes, indicating a change in the relative amount of the pure phase TMA_2PbCl_4 with respect to the iodide–chloride mixed phase. The overall behavior can be explained by the different ionic radius of the halide as well as by the different stiffness of the organic cation which overall impact on the deformability of the entire inorganic lattice. I and Br, and similarly Br and Cl, have similar radii (≈0.219 nm for I^-, 0.196 nm for Br^- and 0.181 nm for Cl^-), therefore the complementary halide is readily incorporated in the crystal lattice without large structural change, resulting in the formation of a single crystalline phase. Such incorporation tolerance is no longer occurring in the case of I–Cl mixture, in which there is the greatest disparity in ionic size. In TEA-based materials (Figure 2c), the broadening of the peak masks distinct phases, which are clearly visible in the TMA-based mixed systems (Figure 2d). Here, the two peaks at 6.2° and 5.7° manifest when Cl-content increases (see gray curve in Figure 2d). These two peaks are assigned to the different phases forming in the material, corroborating the hypothesis based on the absorption results of the formation of distinct iodide–chloride and chlorine rich phases. These phenomena are related to the large difference in the dimension of I^- and Cl^- ionic radius: with TEA, the perovskite inorganic octahedra can still accommodate the Cl^- in a distorted lattice, while TMA, which is more rigid, impedes incorporation of further Cl^-, in agreement with the absorption results. As drawn in the chemical structure in Figure 1a, the main difference between TEA and TMA cations is the presence of one more carbon in the alkyl chain of the TEA molecule, which provides enhanced mobility and rotational freedom along the C—C bond axis. Complementary Raman measurements on TMA_2PbI_4 and TEA_2PbI_4 thin films support this proposition (Figure S3, Supporting Information): a shift of the Raman vibrations to higher frequency is visible for the TEA-based material, which indicates the enhanced flexibility of this species with respect to TMA. Furthermore, recently reported theoretical calculations confirm that the length of the carbon chain has an influence over the rigidity of the spacing moieties, and the equilibrium position that lead and halide atoms assume in the inorganic octahedra

can vary accordingly.[28] It is widely known that hybrid perovskites exhibit unique properties of softness, in which the chemical bonding between metal halide octahedral frameworks and cations is governed by weak ionic and hydrogen bonding.[29,30] The steric hindrance provided by bulky cations such as TEA and TMA therefore play a role: TMA has one methyl group, while TEA has one longer methyl group. TEA with stronger steric hindrance can induce larger Pb–I tilt angles and increases the softness of the perovskite.

Hence, the presence of a more flexible cation such as TEA tends to compensate for the high degree of distortion in the lattice induced by mixed halide compositions, leading to the possibility to incorporate into the iodide–chloride mixed phase a higher amount of Cl^- before the R_2PbCl_4 pure phase starts to segregate. The mechanism is summarized in the cartoon of Figure 2e. This is in line with that reported in the literature in the case of 3D perovskites, in which too high content of Cl^- does not allow the formation of a continuous solid phase,[31] while to the best of our knowledge this is the first observation of this phenomenon for the 2DP. In addition, we note that no 3D perovskite has been successfully stabilized with large Cl content, contrarily to that achieved here for the 2DP, highlighting the increased tunability of the 2DP systems.

2.3. Photoluminescence Properties and Mapping

To further explore this concept, we investigate the emission properties of the chlorine-rich mixed systems. In **Figure 3**a,b we show the UV–vis absorption and the photoluminescence (PL) spectra of the TEA_2PbICl_3 and the TMA_2PbICl_3, respectively. Notably, as shown in Figure S11 of the Supporting Information, upon light irradiation for a period of 60 min PL signal remains stable, excluding then the hypothesis of photoinduced degradation and/or ionic segregation. From the absorption spectra of both materials multiple peaks related to the different phases are evident. The main absorption takes place in the UV, ≈320 nm, and is related to the Cl-rich phase, making the film transparent to the human eye (see the photos in the inset of Figure 3). PL spectra of TEA_2PbICl_3 and TMA_2PbICl_3 show a green light emission centered at 500 and 516 nm, respectively; such peaks are assigned to the emission from the iodide-rich phase. Again, as for the absorption, the PL of TEA-based system is slightly blueshifted with respect to the pure iodide phase, while the emission of the TMA-one is almost identical to the pure iodide composition (see by comparison the dashed line related to the emission of the pure iodide R_2PbI_4 in Figure 3), indicating that the iodide content in the TMA case approach 100% while in the TEA case a chlorine incorporation is present. In general, the mixed I–Cl systems have shown a large shift between the main absorption and the emission peak (≈1.30 and 1.38 eV in the case of TEA and TMA systems, respectively) suggesting the phenomenon of funneling of excited species between the two segregated phases. To monitor the energy funneling we have performed PL excitation spectra. Data are reported in Figure S14 of the Supporting Information. PL signal (looking at $\lambda > 350$ nm) does not come only from excitation of the lower-bandgap phase, but from light absorbed throughout all the visible spectra. This suggests that energy transfer happens from higher energy phase into the lowest-bandgap emissive one. Collectively, these results show that the ratio between Cl and I can perturb the microscale phase segregation resulting in a distributed emission (the iodide rich species in this case) which one can controllably vary the halide content.

To better estimate the material phase segregation and understand the microscale distribution of the emissive species we combined hyperspectral PL imaging and elemental mapping. **Figure 4**a,b shows the PL maps for TEA_2PbICl_3 and TMA_2PbICl_3 perovskite thin films at the wavelength corresponding to their maximum PL intensity. The PL spectra are centered at ≈500 nm for TEA_2PbICl_3 and 516 nm for TMA_2PbICl_3, with local variations in intensity on the micrometer scale. The maps show that the PL emission from TMA_2PbICl_3 is spatially more heterogeneous compared to the TEA. This is consistent with the

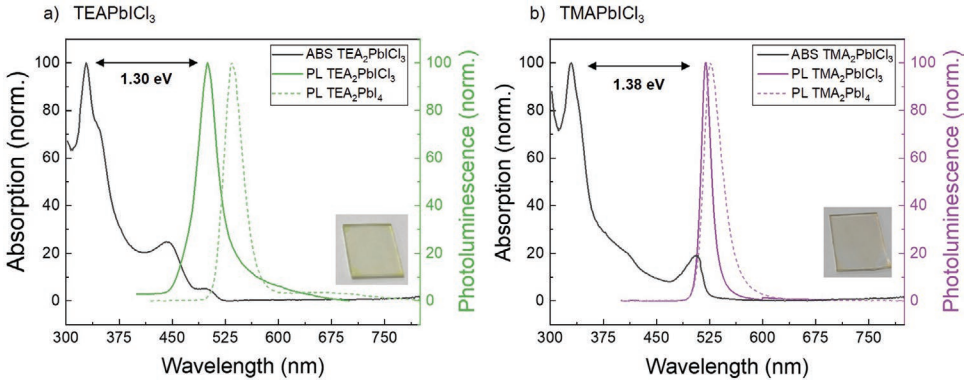

Figure 3. a,b) Optical properties of the TEA_2PbICl_3 (a) and TMA_2PbICl_3 (b) materials in terms of absorption (black line) and photoluminescence (colored continuous line). The presence of multiphases in the materials determines an important shift of 1.30 eV (1.38 eV) represented by the black arrows and defined as the difference between the main absorption peak at 328 nm (329 nm) of the material and its light emission peak centered at 500 nm (516 nm) for the TEA-based (TMA-based) mixed iodide–chloride material. The dotted lines represent the photoluminescence of the pure iodide-based 2DP for the cations considered: the signal of the iodide–chloride mixtures is slightly blueshifted because of the presence of Cl inside the emitting phase of these materials. The main absorption of the material in the UV-region of the light spectra determine the transparent appearance of the deposited films to the human eye, as shown in the inset photos. The PL signal of the R_2PbICl_3 samples has been collected using 300 nm excitation, while the pure iodide materials by using a 405 nm excitation source (see the Experimental Section).

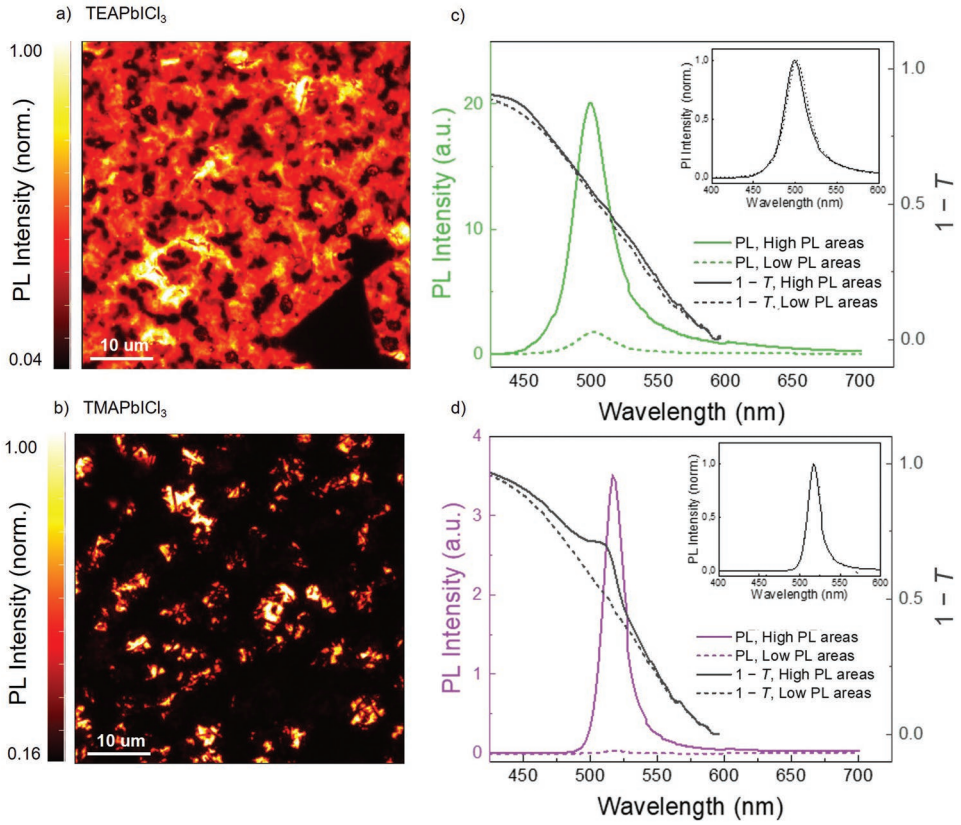

Figure 4. a,b) Hyperspectral photoluminescence maps for TEA_2PbICl_3 (a) and TMA_2PbICl_3 (b) perovskite thin films at emission wavelength of 500 and 516 nm, respectively. c,d) The mean photoluminescence spectra (green and purple curves) and $1 - T$ spectra (black curves) spatially integrated from the high PL (solid lines) and low PL (dotted lines) areas of the PL maps in (a) and (b). (The insets show the normalized PL spectra from bright, solid, and dark areas, dashed.) All the PL maps are taken using 405 nm laser excitation with ≈200 mW cm^{-2} intensity. A calibrated white light source with an intensity of 100 mW cm^{-2} is used for measuring transmittance. PL maps are normalized to the maximum value of the map. The dark shapes in the maps are gold particles deposited as fiducial markers for spatial correlation between PL imaging and elemental mapping. All measurements were performed in an ambient atmosphere.

structural and optical data analyses, in which TEA has a more flexible framework with respect to TMA, and hence propensity to form a more spatially homogeneous mixed I–Cl phases. We note that the PL spatial distribution is more homogeneous for the iodide/bromide mixture, compared to the iodide/chloride for both the TEA and TMA compositions, suggesting we have more segregated regions in the case of iodide/chloride (see Figures S4 and S5 of the Supporting Information for the PL maps of all compositions and Figure S6 of the Supporting Information for spatially integrated PL spectra).

Figure 4c,d shows the mean PL spectra (green and purple curves) spatially averaged from the brighter (solid lines) and darker (dotted lines) regions of the PL maps for both the TEA_2PbICl_3 and TMA_2PbICl_3 compositions. The black curves show the mean 1 – transmittance ($1 - T$) spectra for the same films, which will be discussed later. We observe that though the PL count is significantly higher for the bright areas in comparison with the dark areas, both regions exhibit similar emission peak position (see the insets of Figure 4c and d for normalized spectra). This huge difference (factor of 100 for TMA_2PbICl_3 and 10 for TEA_2PbICl_3) in the PL intensity, and nearly identical PL emission energy, suggests that the I-rich sites are the emissive sites of these films. This indicates a preferential energy transfer path is created toward the lower-bandgap I-rich regions, responsible for the light emission. In order to assess the local variations in the emission to the local optical properties and chemical composition, we measured local reflectance and transmittance spectra of the films from the same area with using a calibrated white light source. Figures S4 and S5 of the Supporting Information show the reflectance and transmittance maps for all the compositions at the wavelength of their maximum PL intensity. We assess the local absorption of the perovskite films through plotting the mean $1 - T$ spectra spatially integrated from the bright and dark regions of the PL maps, assuming that the reflectance has less contribution to absorption (the black curves in Figure 4c,d). For the TMA_2PbICl_3 composition (Figure 4d), we see that the brighter regions of the PL maps have a prominent low-energy shoulder in their $1 - T$ spectra (solid line) at ≈500 nm which is absent in the spectra in darker PL areas (dotted line), which corresponds to the absorption peak of iodide-rich phase (Figure 1). For TEA_2PbICl_3, the $1 - T$ spectra difference (the black curves in Figure 4c) for bright and dark regions of the PL maps is not as significant as in the TMA case. This is again consistent with the structural and optical measurements, suggesting a more homogeneous mixed I–Cl phase for the TEA compositions.

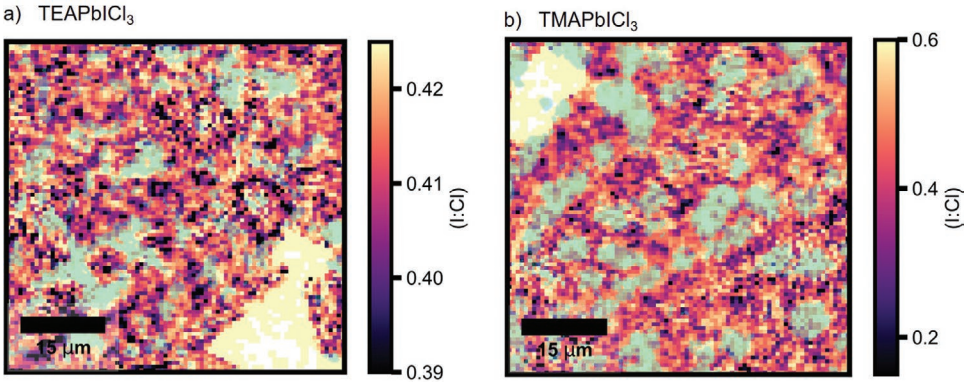

Figure 5. a,b) SEM–EDX maps of iodine:chlorine (I:Cl) peak intensity ratio overlaid with the regions of relatively high photoluminescence intensity (green areas) at peak emission wavelengths for TEA_2PbICl_3 (500 nm) (a) and TMA_2PbICl_3 (516 nm) (b). The yellow shapes in the maps are gold particles deposited as fiducial markers to guide spatial correlation between PL imaging and elemental mapping. The PL maps are taken using 405 nm laser excitation with ≈200 mW cm^{-2} intensity and the measurements were performed in an ambient atmosphere.

In order to further probe the chemical origin of such emissive phases, we used scanning electron microscopy imaging and energy-dispersive X-ray spectroscopy (SEM–EDX) to map the chemical distribution of these films on the same scan areas as the photoluminescence measurements. **Figure 5** shows the SEM–EDX maps of iodine to chlorine (I:Cl) ratio overlayed with the regions that have the highest photoluminescence intensity at the peak emission wavelength (green regions in the maps) for the TEA_2PbICl_3 (Figure 5a) and TMA_2PbICl_3 films (Figure 5b) (see the SEM–EDX maps of the elements in Figures S7 and S8, Supporting Information). From the I:Cl ratio maps, we observe that this ratio changes in a much smaller range for the TEA_2PbICl_3 (from 0.39 to 0.42) compared to TMA_2PbICl_3 (from 0.2 to 0.6) films. This directly shows the formation of a more homogeneous I:Cl mixture for the TEA composition. The I:Cl ratio maps overlayed with the photoluminescence maps (green areas), for both the TMA and TEA compositions, show that there is a clear spatial correlation between the PL intensity and the iodide to chloride ratio maps. This finding highlights the fact that the regions with the highest emission are more iodide-rich, even in the TEA_2PbICl_3 compositions where we have small differences in the Cl:I ratio through the film. We note that the iodide–chloride heterogeneity is in the micrometer range, while the morphological grains are much smaller up to the order of tens of nanometers in size (see Figure S9 of the Supporting Information for the SEM images from the same area, and Figure S10 of the Supporting Information for SEM images of all other compositions). Therefore, the distribution of iodide or chloride regions is not limited by the size and shape of the grains.

Altogether, the imaging of the emission and chemical mapping allows us to demonstrate that a careful control of the halide mixture in 2DP can drive a microscale distribution of phases. As a result, energy transfer paths from the higher-bandgap phase to the lower-bandgap region happens leading to redshifted emission. This approach proves a robust design method for the fine tuning of the emission wavelength allowing for the creation of a new set of transparent materials which can emit in the visible region.

3. Conclusion

Our work demonstrates that modifications over halides composition and organic cation structure are powerful tools to control not only the optical properties (e.g., bandgap) of the material, but also their spatial microscale segregation. Furthermore, we demonstrated how by playing with halide composition and organic moieties, it is possible to control the microscale segregated domains' size and their emission distribution. Using iodide–chloride mixtures leads to the formation of a transparent material with intense green emission. By changing the structure of the organic cation implemented in the 2DP, the microscale phase distribution can be varied and, accordingly, their emission wavelength. Further understanding of these phenomena, as well as the comprehension of the effects that different processes and solvents would have on the microscale segregation, is crucial for the proper engineering of this class of materials. The 2DPs here reported could be further exploited, paving the way for new generation technologies, which appear transparent to human-eye, such as luminescent solar concentrator, tunable LEDs, transparent screens or tools for cryptography. Additionally, the fine control over the spatial segregation could enable the formation of self-assembly of pixels for LED screens on controllable length scales, with domains of different composition that could lead to multiphase materials with multicolor emission.

4. Experimental Section

Materials Synthesis: All the solvents and chemicals were used as purchased without further purification. *N*,*N*-Dimethylformamide (anhydrous 99.9%, DMF), dimethyl sufoxide (anhydrous 99.9%, DMSO), ethanol (EtOH), diethyl ether, chlorobenzene (anhydrous 99.8%, CB), acids in aqueous solution (HI, HBr, HCl), and lead chloride (99.999%, $PbCl_2$) were purchased from Sigma-Aldrich. Lead iodide (99.99%, PbI_2) and lead bromide (99.99%, $PbBr_2$) were purchased from TCI.

Synthesis of Thiophene-Based Cations: Thiophene-based ammonium salts were synthesized following a protocol previously reported for TEA·HI and TMA·HI.[27] A proper amount of 2-Thiophene alkylamine (TEA or TMA) was dissolved in ethanol to obtain a 1.0 M solution. The solution was cooled at 0 °C and a 1:1 aqueous HX (1.1 equivalents of

HI, HBr, or HCl) was added dropwise. The mixture was left to gradually return to room temperature under continuous stirring. Then, an excess of cooled diethyl ether was poured in, inducing the precipitation of the corresponding thiophene salts. The precipitate was collected by vacuum filtration on Buchner and plenty washed with cooled diethyl ether, obtaining white solids (yields ≈ 70–80%).

Perovskite Thin-Film Formation: The as prepared thiophene-based cations (R = TEAX, TMAX, X = I, Br, Cl) were transferred in an Ar_2 filled glovebox, where all the other chemicals were stored, for the precursor solution preparation. PbI_2, $PbBr_2$, and $PbCl_2$ solutions in DMF:DMSO = 0.78:0.22 were prepared with a 0.25 M concentration by stirring overnight at 60 °C. For the 2D perovskite (n = 1) with pure halides composition (R_2PbX_4 and R_2PbX_4) the desired lead-halide solution was used to dissolve the corresponding thiophene cation salt with 1:2 molar ratio. For the mixed halides compositions ($R_2PbX_{4-y}X'_y$, X = I, Br, Cl) two different PbX_2 solutions were mixed in different volume ratio and used to dissolve the thiophene salt in order to obtain the final desired stoichiometry (the total Pb to R molar ratio is still 1:2). The thiophene salts were dissolved easily just by stirring the solutions, they were not heated up further.

The as prepared solutions were used to form the 2D perovskite thin film on quartz glass substrates. Quartz glass substrates were washed in two sequential steps by sonicating them 15 min in acetone and isopropyl alcohol; then a 15 min O_2 plasma cleaning treatment was done. The substrates were transferred in a N_2 filled glovebox (H_2O < 0.1 ppm, O_2 < 0.1 ppm) for the spin-coating process. 60 µL of the precursor solution were spread on top of the 2.5 × 2.5 cm^2 substrate and a two steps spin-coating process was carried out: 2000 rpm, 500 rpm s^{-1} acceleration for 12″ and 5000 rpm, 2000 rpm s^{-1} acceleration for 30″. Chlorobenzene was added as an antisolvent 15″ before the end of the spin-coating process. The films were then annealed for 30 min at 100 °C.

Materials Characterization: UV–Vis Absorption: The absorption spectra of the perovskite thin films were collected using a UV–NIR spectrophotometer from Perkin Elmer (Lambda1050+).

Photoluminescence: The photoluminescence spectra of the perovskite thin films were collected using a customized optical setup in which the excitation was provided by high-power LED at 300 nm (405 nm) while the luminescence was analyzed with an interferometer (GEMINI by Nireos) and recorded with a single photon detector (IDQuantique) coupled with a Time Tagger (Swabian Instrument). The scan has been performed in the range of 320–800 nm (420–800 nm).

X-ray Diffraction: XRD measurements were performed with a Bruker D8Advance diffractometer with a non-monochromated Cu-source for the X-ray radiation. The 3°–35° 2θ scan lasted ≈30 min with a step size about 0.0250°. All the measurements were performed at room temperature.

Photoluminescence Microscopy: PL maps were acquired using a wide-field, hyperspectral imaging microscope (Photon etc. IMA VIS). A front-illuminated, low-noise CCD camera was thermoelectrically cooled down to 0 °C. The PL excitation source was a power-tunable 405 nm laser with an intensity of 200 mW cm^{-2} (spot size diameter is ≈150 µm). In order to block the 405 nm laser reflection, a 420 nm long-pass filter was placed in the detection pathway. For the PL maps, the detection wavelength range was from 400 to 700 nm, to measure all acquisition of the PL spectrum. The step size was set at 1 nm and the dwell time at 1 s. For the transmittance and reflectance measurements, a calibrated white-light source at 100 mW cm^{-2} intensity and the same low-noise CCD camera were used. The detection wavelengths were from 400 to 1000 nm, with a step size = 2 nm and dwell time = 0.5 s. All data were acquired in ambient atmospheric conditions.

Raman Spectroscopy: Raman measurement was performed with a Horiba Jobin–Yvon T64000 triple-monochromator spectrometer operating in a subtractive mode equipped with a Symphony LN2-cooled CCD detector, 600 gr mm^{-1} holographic gratings, an Olympus BH-41 optical microscope with a 50× long-working distance objective, and a coherent Ar^+ laser at the Department of Earth Sciences of the University of Pavia (Italy). The red laser (633 nm) and ≈1% of the total laser power were used to acquire data (calculated laser excitation density D is ≈100 mW cm^{-2}), precautioning not to degrade the perovskite sample.

Scanning Electron Microscopy and Energy-Dispersive X-Ray Spectroscopy: SEM images in Figure S9 of the Supporting Information were acquired using an FEI Nova NanoSEM in secondary electron mode with an Everhart-Thornley detector. The electron gun high voltage was set at 2 kV and the beam current was 27 pA. Hyperspectral EDX data were acquired using the same instrument and a Bruker XFlash EDX detector. The electron gun high voltage was set at 10 kV and the beam current was 200 pA. EDX data were denoised with principal component analysis and further processed in HyperSpy. The Br-L_α, I-L_α, and Pb-M_α lines were used to map the distributions of Br, I, and Pb, respectively. For the SEM Images in Figure S10 of the Supporting Information, another scanning electron microscope (Merlin) was employed to examine surface morphology of the perovskite film. The electron beam was accelerated to 3 kV, and an in-lens detector was used.

Supporting Information

Supporting Information is available from the Wiley Online Library or from the author.

Acknowledgements

A.Z and Z.A.-G. contributed equally to this work. A.Z. and G.G. acknowledge the "HY-NANO" project that received funding from the European Research Council (ERC) Starting Grant 2018 under the European Union's Horizon 2020 research and innovation programme (Grant Agreement No. 802862). The authors acknowledge the project GO for IT that received funding from Fondazione CRUI. G.G. acknowledges the Project EXPRESS that received funding from the program FARE Ricerca In Italia (No. R18ENKMTA3). The authors acknowledge Prof. Matteo Alvaro and Dr. Stefania Righetto for the use of the Raman facility at the Department of Earth Sciences of the University of Pavia (Italy). G.G. acknowledges Dr. Albertus Sutanto and Dr. Valentin Queloz for fruitful discussion. K.F. acknowledges a George and Lilian Schiff Studentship, Winton Studentship, the Engineering and Physical Sciences Research Council (EPSRC) studentship, Cambridge Trust Scholarship, and Robert Gardiner Scholarship. F.U.K. thanks the Jardine Foundation and Cambridge Trust for a doctoral scholarship. This work received funding from the European Research Council under the European Union's Horizon 2020 research and innovation programme (HYPERION – Grant Agreement No. 756962). The authors acknowledge the EPSRC (EP/R023980/1) for funding. S.D.S. acknowledges the Royal Society and Tata Group (UF150033).

Open Access Funding provided by Universita degli Studi di Pavia within the CRUI-CARE Agreement.

Conflict of Interest

The authors declare no conflict of interest.

Data Availability Statement

Research data are not shared.

Keywords

2D perovskites, halide mixtures, light emission, segregation, transparent light-emitting devices, tunability

Received: July 31, 2021
Revised: September 10, 2021
Published online:

[1] Best Research-Cell Efficiency Chart, https://www.nrel.gov/pv/cell-efficiency.html (accessed: August 2021).
[2] H. Lu, Y. Liu, P. Ahlawat, A. Mishra, W. R. Tress, F. T. Eickemeyer, Y. Yang, F. Fu, Z. Wang, C. E. Avalos, B. I. Carlsen, A. Agarwalla, X. Zhang, X. Li, Y. Zhan, S. M. Zakeeruddin, L. Emsley, U. Rothlisberger, L. Zheng, A. Hagfeldt, M. Grätzel, *Science* **2020**, *370*, 8985.
[3] K. Lin, J. Xing, L. N. Quan, F. P. de García de Arquer, X. Gong, J. Lu, L. Xie, W. Zhao, D. Zhang, C. Yan, W. Li, X. Liu, Y. Lu, J. Kirman, E. H. Sargent, Q. Xiong, Z. Wei, *Nature* **2018**, *562*, 245.
[4] G. Pacchioni, *Nat. Rev. Mater.* **2021**, *6*, 108.
[5] L. N. Quan, F. P. de García de Arquer, R. P. Sabatini, E. H. Sargent, *Adv. Mater.* **2018**, *30*, 1801996.
[6] M. Yuan, L. N. Quan, R. Comin, G. Walters, R. Sabatini, O. Voznyy, S. Hoogland, Y. Zhao, E. M. Beauregard, P. Kanjanaboos, Z. Lu, D. H. Kim, E. H. Sargent, *Nat. Nanotechnol.* **2016**, *11*, 872.
[7] G. Grancini, M. K. Nazeeruddin, *Nat. Rev. Mater.* **2019**, *4*, 4.
[8] C. Katan, N. Mercier, J. Even, *Chem. Rev.* **2019**, *119*, 3140.
[9] D. B. Straus, C. R. Kagan, *J. Phys. Chem. Lett.* **2018**, *9*, 1434.
[10] Y. Zhai, S. Baniya, C. Zhang, J. Li, P. Haney, C.-X. Sheng, E. Ehrenfreund, Z. V. Vardeny, *Sci. Adv.* **2017**, *3*, 1700704.
[11] A. Xie, F. Maddalena, M. E. Witkowski, M. Makowski, B. Mahler, W. Drozdowski, S. V. Springham, P. Coquet, C. Dujardin, M. D. Birowosuto, C. Dang, *Chem. Mater.* **2020**, *32*, 8530.
[12] J. Cao, Z. Guo, S. Zhu, Y. Fu, H. Zhang, Q. Wang, Z. Gu, *ACS Appl. Mater. Interfaces* **2020**, *12*, 19797.
[13] L. Pedesseau, D. Sapori, B. Traore, R. Robles, H.-H. Fang, M. A. Loi, H. Tsai, W. Nie, J.-C. Blancon, A. Neukirch, S. Tretiak, A. D. Mohite, C. Katan, J. Even, M. Kepenekian, *ACS Nano* **2016**, *10*, 9776.
[14] C. Li, J. Wei, M. Sato, H. Koike, Z.-Z. Xie, Y.-Q. Li, K. Kanai, S. Kera, N. Ueno, J.-X. Tang, *ACS Appl. Mater. Interfaces* **2016**, *8*, 11526.
[15] N. Kitazawa, *Mater. Sci. Eng., B* **1997**, *49*, 233.
[16] N. Kitazawa, *Jpn. J. Appl. Phys.* **1996**, *35*, 6202.
[17] N. Kitazawa, K. Enomoto, M. Aono, Y. Watanabe, *J. Mater. Sci.* **2004**, *39*, 749.
[18] G. Lanty, K. Jemli, Y. Wei, J. Leymarie, J. Even, J.-S. Lauret, E. Deleporte, *J. Phys. Chem. Lett.* **2014**, *5*, 3958.
[19] M.-G. La-Placa, D. Guo, L. Gil-Escrig, F. Palazon, M. Sessolo, H. J. Bolink, *J. Mater. Chem. C* **2020**, *8*, 1902.
[20] S. Wang, Y. Yao, Z. Wu, Y. Peng, L. Li, J. Luo, *J. Mater. Chem. C* **2018**, *6*, 12267.
[21] P. Cai, X. Wang, H. J. Seo, X. Yan, *Appl. Phys. Lett.* **2018**, *112*, 153901.
[22] L. Mao, Y. Wu, C. C. Stoumpos, B. Traore, C. Katan, J. Even, M. R. Wasielewski, M. G. Kanatzidis, *J. Am. Chem. Soc.* **2017**, *139*, 11956.
[23] P. Pang, G. Jin, C. Liang, B. Wang, W. Xiang, D. Zhang, J. Xu, W. Hong, Z. Xiao, L. Wang, G. Xing, J. Chen, D. Ma, *ACS Nano* **2020**, *14*, 11420.
[24] K.-H. Wang, Y. Peng, J. Ge, S. Jiang, B.-S. Zhu, J. Yao, Y.-C. Yin, J.-N. Yang, Q. Zhang, H.-B. Yao, *ACS Photonics* **2019**, *6*, 667.
[25] S. Yang, Z. Lin, J. Wang, Y. Chen, Z. Liu, E. Yang, J. Zhang, Q. Ling, *ACS Appl. Mater. Interfaces* **2018**, *10*, 15980.
[26] Y. Nah, O. Allam, H. S. Kim, J. I. Choi, I. S. Kim, J. Byun, S. O. Kim, S. S. Jang, D. H. Kim, *ACS Nano* **2021**, *15*, 1486.
[27] A. A. Sutanto, N. Drigo, V. I. E. Queloz, I. Garcia-Benito, A. R. Kirmani, L. J. Richter, P. A. Schouwink, K. T. Cho, S. Paek, M. K. Nazeeruddin, G. Grancini, *J. Mater. Chem. A* **2020**, *8*, 2343.
[28] M. B. Fridriksson, N. van der Meer, J. de Haas, F. C. Grozema, *J. Phys. Chem. C* **2020**, *124*, 28201.
[29] M.-H. Tremblay, J. Bacsa, S. Barlow, S. R. Marder, *Mater. Chem. Front.* **2020**, *4*, 2023.
[30] Y. Miao, Y. Chen, H. Chen, X. Wang, Y. Zhao, *Chem. Sci.* **2021**, *12*, 7231.
[31] S. Colella, E. Mosconi, P. Fedeli, A. Listorti, F. Gazza, F. Orlandi, P. Ferro, T. Besagni, A. Rizzo, G. Calestani, G. Gigli, F. De Angelis, R. Mosca, *Chem. Mater.* **2013**, *25*, 4613.